KSTLE International Journal, Vol. 5, No. 1, June 2004, pp. 14-22

Sub-surface Stress Analysis on Spur Gear Teeth in the EHL Conditions

Young-Pil Koo†, Tae-Wan Kim* and Yong-Joo Cho**

School of Mechanical Engineering, Pukyong National University, Busan, Korea
**Research Institute of Mechanical Technology, Pusan National University, Busan, Korea*
***School of Mechanical Engineering, Pusan National University, Busan, Korea*

Abstract: The sub-surface stress field beneath the gear's contact surface caused by the surface pressure in lubricated condition is analyzed. To evaluate the influence of the clearances between a gear tooth and a pinion tooth on the stress field, two kinds of tooth profile models - conventional cylinder contact model and new numerical model - were chosen. Kinematics of the gear is taken into account to obtain the numerical model which is the accurate geometric clearances between a gear tooth and a pinion tooth. Transient elasto-hydrodynamic lubrication (EHL) analysis is performed to get the surface pressure. The sub-stress field is obtained by using Love's rectangular patch solution. The analysis results show that the sub-surface stress is quite dependent on both the surface pressures and the profile models. The maximum effective stress of the new model is lower than that of the old model. The depth where the maximum effective stress occurs in the new model is not proportional to the intensity of the external load.

Key words: Spur gear, Sub-surface stress, Kinematics, EHL

Introduction

Gears are essential elements to transfer power and are widely applied to most machinery. In accordance with the development of precision machinery, the design technique based on reliability becomes very important on gears[1-2]. To improve reliability, not only gear strength design but also tooth surface design which aims at good functioning of the surface is necessary.

The tooth surface design pertains to tooth geometry design, tooth width profiling, decision of the surface hardening depth, etc. Both the surface pressure distribution and sub-surface stress distribution should be known prior to the tooth surface design. When an external force acts on the gear tooth to transfer power, the contact pressures are generated on the contact surfaces. In the case of non-conformal contact, like gear teeth contact, because the local pressure of the contact area becomes too high, the contact pressures influence the sub-surface stress distribution beneath both the contact area and neighboring area. Therefore, the contact pressure has a great effect on the life of the tooth surface[3-4].

The contact pressures for dry contact whose area can be simplified to an ellipse are obtained from Hertzs exact solutions[5]. Because the contact area of the gear teeth is not elliptic and lubricant exists between the gear teeth, the Hertzs solution cannot be used any more on gear teeth contact.

The contact surface pressure in a lubricated condition can be obtained by elasto-hydrodynamic lubrication (EHL) analysis.

The EHL analysis requires precise geometric clearances between gear teeth because the wedge effect is dominant in pressure distribution[6]. The conventional model for the teeth clearances in the EHL analysis has been approximated to the contact of two cylinders whose radii are set to the radius of curvature at the contact point. But the actual curvature of gear teeth is continuously changing around the contact point. Therefore, the cylinder contact model cannot describe the actual teeth clearances.

In this study, to estimate the sub-surface stress field beneath the contact surface of the spur gear teeth accurately, a procedure to calculate the teeth clearances with consideration of gear kinematics is suggested. The surface pressure distribution between a gear tooth and a pinion tooth is obtained by transient EHL analysis with the aid of the calculated geometric clearances. To analyze the effect of the teeth clearances, the sub-surface stress fields are calculated for two tooth profile models and compared with each other.

Geometric Clearances between Gear Tooth and Pinion Tooth

Figure 1 shows contacting spur gear and pinion with coordinates systems. The clearances between the gear tooth and the pinion tooth should be known prior to the EHL analysis. Because the contact points of the teeth move and the contact radii of curvature change as the gear rotates, the teeth clearances also change over time. By the following procedure, the accurate geometric clearances for a specific time step can be obtained.

1. Tooth profiles of the gear and the pinion are generated by Eq. (1) in local Cartesian coordinates whose origins are located at the center of the gear and the pinion respectively.

†Corresponding author; Tel: 82-51-620-1621, Fax: 82-51-620-1405
E-mail: ypkoo@naver.com

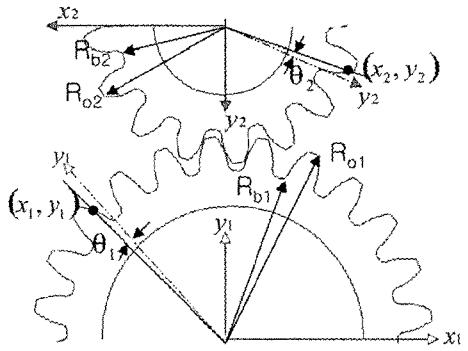

Fig. 1. Schematics of the gear and pinion.

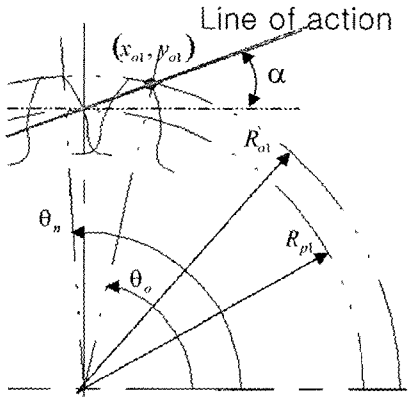

Fig. 2. Setting the initial reference point.

$$x_i = R_{bi}(\theta_i \cos\theta_i - \sin\theta_i)$$
$$y_i = R_{bi}(\cos\theta_i + \theta_i \sin\theta_i) \tag{1}$$

The subscript i equals 1 for gear, 2 for pinion.

The angle range of one side profile between the base radius and the outside radius is:

$$0 \le \theta_i \le \frac{\sqrt{R_{oi}^2 - R_{bi}^2}}{R_{bi}} \tag{2}$$

2. To find the posture of the gear profile and pinion profile at the starting contact point, the gear profile is rotated so that its outermost point meets the intersection of the gear's outside diameter and the line of action as shown in Fig. 2. Cartesian coordinates of the intersection point are:

$$x_{o1} = \frac{-2R_{p1}\tan\alpha + \sqrt{4R_{p1}^2\tan^2\alpha - 4(1+\tan^2\alpha)(R_{p1}^2 - R_{o1}^2)}}{2(1+\tan^2\alpha)}$$
$$y_{o1} = x_{o1}\tan\alpha + R_{p1} \tag{3}$$

Then, pinion profile is rotated until the initial contact point on the pinion profile matches the above intersection point. As shown in Eq. (4), the initial contact point on the pinion profile is the one from which the distance to the origin of the pinion is the same as the distance from the intersection point to the origin.

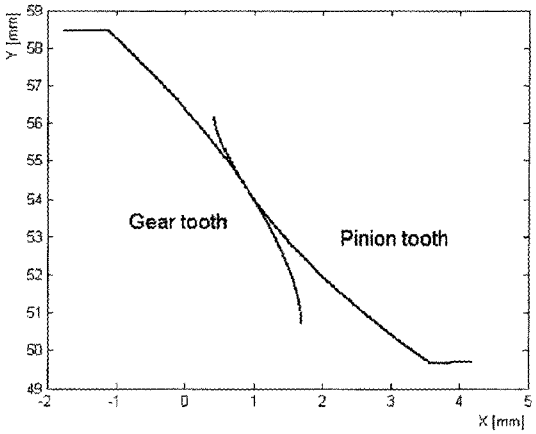

Fig. 3. Configuration of the contacting teeth.

$$\sqrt{x_2^2 + y_2^2} = \sqrt{(-x_{o1})^2 + (R_{p1} + R_{p2} - y_{o1})^2} \tag{4}$$

3. To get the moved profile posture by the successive rotation of the gear and the pinion, the local Cartesian coordinates are converted to the local polar coordinates making use of Eq. (5).

$$r_i = \sqrt{x_i^2 + y_i^2}$$
$$\theta_i = \frac{\pi}{2} + \tan^{-1}\left(-\frac{x_i}{y_i}\right) \quad \forall x_i \le 0, y_i > 0 \tag{5}$$
$$\theta_i = \tan^{-1}\left(\frac{y_i}{x_i}\right) \quad \forall x_i > 0, y_i > 0$$

Several rotation angles are selected along the line of action and the gear and the pinion are rotated stepwise to each other. After each step rotation, the local polar coordinates are converted to the global Cartesian coordinates and the profile data is reserved. Figure 3 shows the configuration of both profiles at the step near the pitch point.

4. To find a contact point of two profiles at each step, the distances between two profiles are calculated. Points in pair whose distance is minimum become contact points numerically.

5. Region for lubrication analysis is set: The inlet region for both the pinion tooth profile and gear tooth profile is the same size, using the contact center as a reference point. In the same way, the outlet region for both profiles is also the same size. Because the grid sizes of the profiles are not even due to the conversion of a polar to a Cartesian coordinate system, the nodes should be rearranged so as to have an even grid size along the original profiles.

6. Finally, the initial clearances are obtained by calculating distances between two mating nodes:

$$h_g = \sqrt{(x_2 - x_1)^2 + (y_2 - y_1)^2} \tag{6}$$

Governing equations

Elasto-hydrodynamic lubrication

The "Reynolds Equation" is adopted to find surface pressure distributions through transient EHL analysis[6]:

$$\frac{\partial}{\partial\xi}\left(\frac{\rho h^3}{\eta}\frac{\partial p}{\partial\xi}\right)+\frac{\partial}{\partial\zeta}\left(\frac{\rho h^3}{\eta}\frac{\partial p}{\partial\zeta}\right) = 12\tilde{u}\frac{\partial(\rho h)}{\partial\xi}+12\frac{\partial(\rho h)}{\partial t} \quad (7)$$

The second term on the right hand side of Eq. (7) is the transient term for variation of density and film thickness with the elapse of time. The dominant effect of the transient term comes from film thickness changes due to movement of the contact point. The entraining velocity is calculated by Eq. (8).

$$\begin{aligned}\tilde{u} &= (u_1+u_2)/2\\ u_1 &= \omega_1(R_{p1}\sin\alpha+x)\\ u_2 &= \omega_2(R_{p2}\sin\alpha-x)\end{aligned} \quad (8)$$

The pressure distribution should satisfy the force equilibrium condition in Eq. (9). The resultant force composed by pressures should be balanced to the external load.

$$w = \iint p\,dxdy \quad (9)$$

At an EHL regime, dependency of viscosity and density on pressure should be considered[7-8]:

$$\eta = \eta_0\left(\frac{6.31\times10^{-5}}{\eta_0}\right)^{1-(1+p/1.96\times10^8)^Z} \quad (10)$$

$$\rho = \rho_0\left(1+\frac{0.6\times10^{-9}p}{1+1.7\times10^{-9}p}\right) \quad (11)$$

Sub-surface stress

The contacting gear tooth can be treated as an elastic half-infinite space because the gear tooth contact area is very small compared with the size of the gear tooth itself. In this case, the sub-surface stress components in the body caused by even normal pressure p_k on a rectangular patch of the surface can be obtained by using Loves solution[9]:

$$\begin{aligned}s_{11,k} &= \frac{1}{2\pi}\left(\frac{\lambda}{\lambda+\mu}\frac{\partial\Lambda}{\partial z}-\frac{\mu}{\lambda+\mu}\frac{\partial^2\Gamma}{\partial x^2}-z\frac{\partial^2\Lambda}{\partial x^2}\right)\\ s_{22,k} &= \frac{1}{2\pi}\left(\frac{\lambda}{\lambda+\mu}\frac{\partial\Lambda}{\partial z}-\frac{\mu}{\lambda+\mu}\frac{\partial^2\Gamma}{\partial y^2}-z\frac{\partial^2\Lambda}{\partial y^2}\right)\\ s_{33,k} &= \frac{1}{2\pi}\left(\frac{\partial\Lambda}{\partial z}-z\frac{\partial^2\Lambda}{\partial z^2}\right)\\ s_{12,k} &= -\frac{1}{2\pi}\left(\frac{\lambda}{\lambda+\mu}\frac{\partial^2\Gamma}{\partial x\partial y}+z\frac{\partial^2\Lambda}{\partial x\partial y}\right)\end{aligned} \quad (12)$$

$$\begin{aligned}s_{23,k} &= -\frac{1}{2\pi}\left(z\frac{\partial^2\Lambda}{\partial x\partial z}\right)\\ s_{31,k} &= -\frac{1}{2\pi}\left(z\frac{\partial^2\Lambda}{\partial z\partial x}\right)\end{aligned}$$

where,

$$\lambda = \frac{Ev}{(1+v)(1-2v)},\quad \mu = \frac{E}{2(1+v)}$$

Γ and Λ are potential functions defined as:

$$\begin{aligned}\Gamma &= \iint p_k\log(z+l)d\xi d\zeta\\ \Lambda &= \iint\frac{p_k}{l}d\xi d\zeta\\ l &= \sqrt{(x-\xi)^2+(y-\zeta)^2+z^2}\end{aligned} \quad (13)$$

Numerical Analysis

Analysis procedure and conditions

Figure 4 represents the overall analysis procedure. First, the geometric teeth clearances are calculated with consideration of the rotational motion of both the gear and the pinion. Next, the EHL analysis is performed to get the surface pressure in a lubricated condition. To get converged results from EHL analysis, some attention should be paid to the analysis procedure because the governing equations are non-linear and

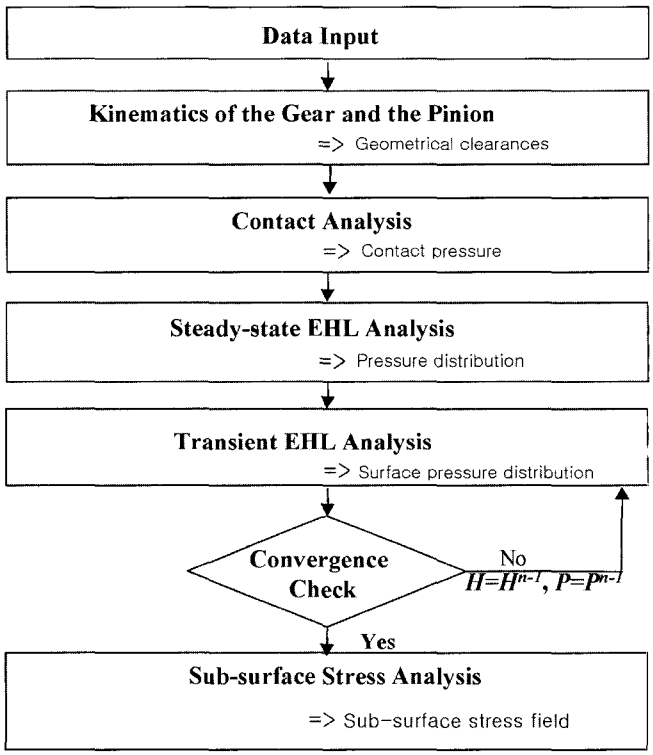

Fig. 4. Overall analysis procedure

Table 1. Properties of the lubricant

Grade	SAE30
Absolute viscosity	0.07 Ns/m^2 @80
Pressure-viscosity coefficient	1.51×10^{-8} m^2/N
Roelands coefficient	0.4223

are apt to diverge accordingly. Newton-Rapson method is adopted for the analysis, as it comparatively converges well in this case. But stability of the analysis with the Newton-Rapson method is quite dependent on the initial guess. One of the remedies to obtain stability is to narrow the differences between the initial guess and the final solution. For this, contact analysis is carried out first and the contact pressure distribution that satisfies the equilibrium condition is used for the initial pressure of steady EHL analysis[10]. And the pressure distribution from the result of steady EHL analysis is set to the initial pressure of transient EHL analysis. Finally, the sub-surface stress is calculated by adopting the surface pressure in a lubricated condition as input data.

The object of the analysis is the involute spur gear: module of 4.5 mm, pressure angle of 20 degrees, tooth width of 20 mm. Number of teeth are 24 and 16 and angular speeds are 460 min^{-1} and 2190 min^{-1} for the gear and the pinion respectively. The yield strength of the material is 830 MPa, the longitudinal modulus of elasticity is 220 GPa, Poisson's ratio is 0.3. The grid sizes are 0.0179 mm($2a$) in rolling and sliding direction, 0.50 mm($2b$) in tooth width direction, and 0.0045 mm ($a/2$) in tooth depth direction respectively. Properties of the lubricant for EHL analysis are listed on Table 1.

The friction is neglected because gears are operated in a lubricated condition and the analysis zone is confined to near the pitch point where the sliding is limited. To display the differences according to profile models clearly, the effects of the surface roughness were not taken into account.

Tooth profile models

Though the tooth geometry is a continuous involute tooth profile, discrete values of tooth geometry are introduced in the numerical analysis. In this study, two kinds of tooth profile model are analyzed from EHL pressure distribution and sub-surface stress distribution. One is the conventional cylinder contact profile model and another is a new numerical profile model. The cylinder contact profile model shows the clearances between two contacting cylinders whose radii are the radius of curvature at the contact point on a gear tooth and a pinion tooth[11]. The equivalent radius of the cylinder contact

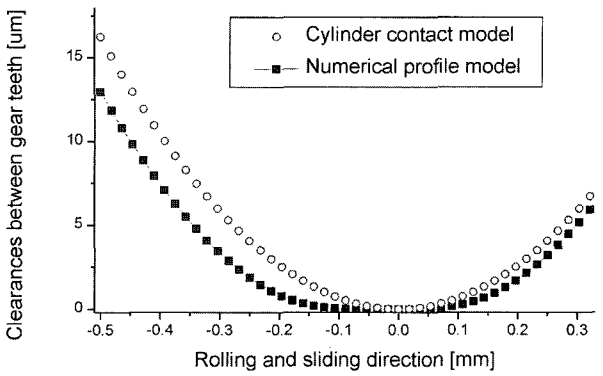

Fig. 5. Comparison of two profile models.

profile model is defined by:

$$R = \left(\frac{1}{R_1} + \frac{1}{R_2}\right)^{-1} \tag{14}$$

Because the actual curvature of gear teeth is continuously changing around the contact point, the cylinder contact model is slightly problematic. The new numerical profile model aims at obtaining the actual teeth clearances the procedure of which is described in Chapter 3 of this paper. Figure 5 shows the clearances for both profile models.

EHL analysis

Dimemsionless parameters are:

$$X = \frac{\xi}{R},\ Y = \frac{h}{R},\ H = \frac{h}{R},\ \bar{\eta} = \frac{\eta}{\eta_0},\ \bar{\rho} = \frac{\rho}{\rho_0},\ P = \frac{p}{E},$$

$$U = \frac{\eta_0 \tilde{u}}{ER},\ T = \frac{\omega_1 t}{2\pi},\ V = \frac{\omega_1 \eta_0}{\pi E}$$

By making use of the dimensionless parameters, Eq. (7) is expressed in dimensionless form:

$$\frac{\partial}{\partial X}\left(\frac{\bar{\rho}H^3}{\bar{\eta}}\frac{\partial P}{\partial X}\right) + \frac{\partial}{\partial Y}\left(\frac{\bar{\rho}H^3}{\bar{\eta}}\frac{\partial P}{\partial Y}\right) = 12U\frac{\partial(\bar{\rho}H)}{\partial X} + 6V\frac{\partial(\bar{\rho}H)}{\partial T} \tag{15}$$

The effective radius of the first time step is adopted as the reference length for the dimensionless film thickness of the whole time steps.

Equation (16) expresses finite difference approximation by adopting central differences for space and backward differences for time.

$$\begin{aligned} f_{i,j} = {} & \frac{1}{2}\left\{\left(\frac{\bar{\rho}H^3}{\bar{\eta}}\right)_{i+1,j} + \left(\frac{\bar{\rho}H^3}{\bar{\eta}}\right)_{i,j}\right\}\frac{P_{i+1,j} - P_{i,j}}{\Delta X^2} - \frac{1}{2}\left\{\left(\frac{\bar{\rho}H^3}{\bar{\eta}}\right)_{i,j} + \left(\frac{\bar{\rho}H^3}{\bar{\eta}}\right)_{i-1,j}\right\}\frac{P_{i,j} - P_{i-1,j}}{\Delta X^2} \\ & + \frac{1}{2}\left\{\left(\frac{\bar{\rho}H^3}{\bar{\eta}}\right)_{i,j+1} + \left(\frac{\bar{\rho}H^3}{\bar{\eta}}\right)_{i,j}\right\}\frac{P_{i,j+1} - P_{i,j}}{\Delta Y^2} - \frac{1}{2}\left\{\left(\frac{\bar{\rho}H^3}{\bar{\eta}}\right)_{i,j} + \left(\frac{\bar{\rho}H^3}{\bar{\eta}}\right)_{i,j-1}\right\}\frac{P_{i,j} - P_{i,j-1}}{\Delta Y^2} \\ & - 6U\frac{\bar{\rho}_{i+1,j}H_{i+1,j} - \bar{\rho}_{i-1,j}H_{i-1,j}}{\Delta X} - 6V\left[H_{i,j}\left(\frac{\partial\bar{\rho}}{\partial P}\right)_{i,j}\frac{P_{i,j} - P_{i,j}^{n-1}}{\Delta T} + \bar{\rho}_{i,j}\frac{H_{i,j} - H_{i,j}^{n-1}}{\Delta T}\right] \end{aligned} \tag{16}$$

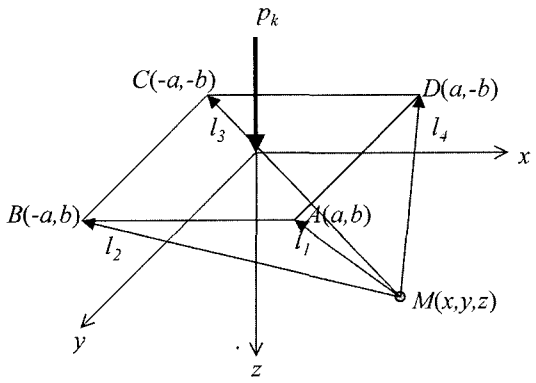

Fig. 6. Load on a rectangular patch and coordinate system.

where, '*n-1*' is the superscript representing a time-step that is immediately prior to the present time-step. The contact surface pressures that keep equilibrium with the external force are obtained by using the Newton-Rapson method to solve for the finite difference of Eq. (16).

Sub-surface stress analysis

The surface pressures that were obtained from EHL analysis are introduced to the input normal pressures on the sub-surface stress analysis. The surface acting normal pressure is divided into n rectangular patches. One of the rectangular patches is shown on Fig. 6. Locating the origin of the coordinates at the center of the patch, the distances from point M in the body and four corners of the patch are calculated by Eq. (17).

$$\begin{aligned} l_1 &= \sqrt{(a-x)^2+(b-y)^2+z^2} \\ l_2 &= \sqrt{(a+x)^2+(b-y)^2+z^2} \\ l_3 &= \sqrt{(a+x)^2+(b+y)^2+z^2} \\ l_4 &= \sqrt{(a-x)^2+(b+y)^2+z^2} \end{aligned} \tag{17}$$

The partial derivatives in Eq. (12) are calculated by using Love's solutions[9]. The stress components in the body caused by the normal pressure acting on only one rectangular patch are calculated by Eq. (12). By accumulating the influence of the whole surface pressure on the stress components in the body, the sub-surface distribution field is obtained. Namely, the stress components in the body are expressed by:

$$\sigma_{ij} = \sum_{k=1}^{n} s_{ij,k} \tag{18}$$

Here, $s_{ij,k}$ is the stress component at a point in the body caused by a specific normal pressure p_k.

Analysis Result and Discussion

The EHL analysis results are shown first. Figure 7 and Fig. 8 demonstrate the pressure distribution of the contact regions between the teeth for the low load step and high load step

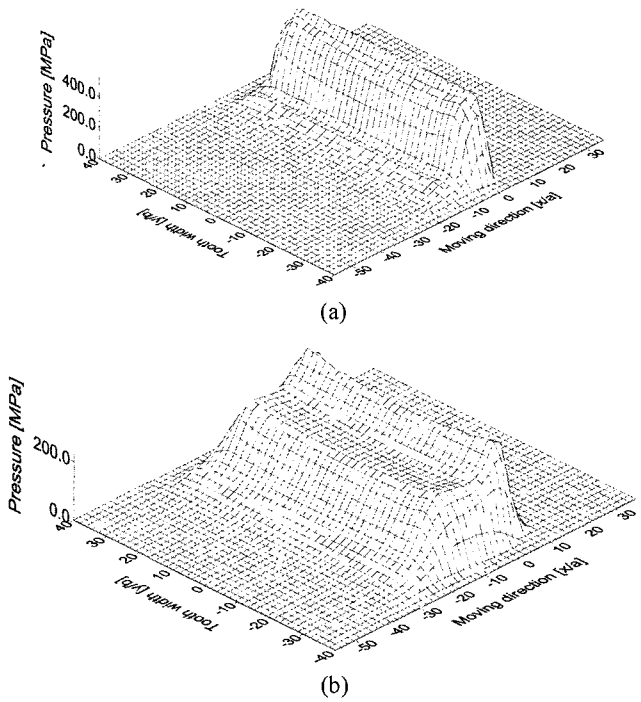

Fig. 7. Surface pressure at load of 970 N (low). (a) Cylinder contact model (b) Numerical profile model.

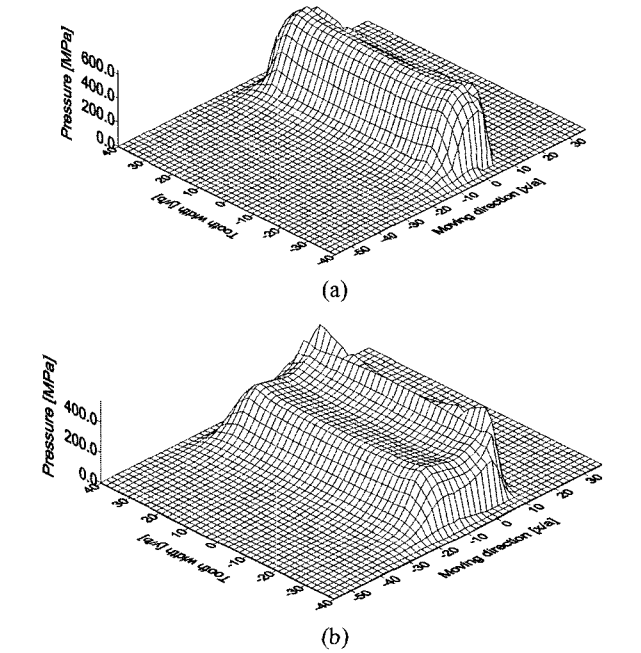

Fig. 8. Surface pressure at load of 1540 N (high). (a) Cylinder contact model (b) Numerical profile model.

respectively. They indicate the pressures in tooth width direction as well as rolling and sliding direction. The axis title, moving direction, means rolling and sliding direction of tooth profile. The maximum pressure emerges on both edges of the tooth width at the outlet region. For the cylinder contact profile model, pressure peaks at the outlet region, which is a representative phenomenon in EHL regime. For the numerical

profile model, besides the pressure spike at the outlet region, the pressure at the inlet region is slightly higher than that of the center region.

The sub-surface stress distributions are explained with the aid of von Mises' effective stress equation[12]:

$$\sigma_e = \sqrt{3\left[\sigma_{12}^2 + \sigma_{23}^2 + \sigma_{31}^2 + \frac{1}{6}\{(\sigma_{11} - \sigma_{22})^2 + (\sigma_{22} - \sigma_{33})^2 + (\sigma_{33} - \sigma_{11})^2\}\right]} \quad (19)$$

Figure 9 and Fig. 10 show the effective stress distribution on a horizontal plane where the maximum effective stress occurs in the body for both low load and high load. The distribution pattern resembles that of the surface pressure. The distribution area of effective stress for the cylinder contact profile model is narrow because the contact area is small. The maximum effective stress of the cylinder contact model is higher than that of the numerical profile model.

Figure 11 and Fig. 12 indicate the contour of the effective stress distribution on a vertical plane where the maximum effective stress occurs in the body for both low load and high load. The values of contour lines are the ratio of effective stress to yield strength S. For the cylinder contact profile model, the position where maximum effective stress occurs is close to the center of the initial contact point in rolling and sliding direction. The vertical distance from the surface to the position where maximum effective stress occurs in depth direction is increased with the increasing load, which complies with Hertzs theory[3]. For the numerical profile model, the position where maximum effective stress occurs is moved to the outward in rolling and sliding direction. The horizontal distance from the center to the position where maximum effective stress occurs is increased with the increasing load. The vertical distance from the surface to the position where maximum effective stress occurs in depth direction is decreased with the increasing load, which is contrary to the general case. The reason why the numerical profile model's sub-surface stress is a different shape can be explained by the following: Because the surface pressures of the numerical profile model have two peak values, like Fig. 7(b), Fig. 8(b), the effects are superimposed on the sub-surface stress field. The sub-surface stress field is widely spread as well because the contact area of the numerical profile model is bigger than that of the cylinder contact profile model.

Figure 13 shows the dimensionless contour plot on horizontal plane where the maximum effective stress occurs in the body for low load. The maximum value of the numerical profile model is 0.189, which is 55% of that of the cylinder contact model. In Fig. 14 for high load, the maximum value of the numerical profile model is 69% of that of the cylinder contact model. The contact area of the cylinder contact model is proportional to the square root of the load. Whereas the contact area of the numerical profile model is wider than that

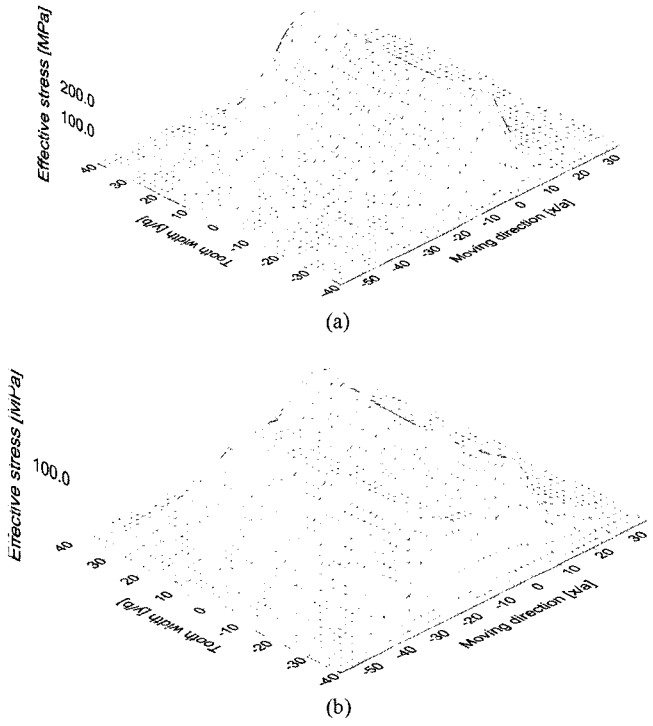

Fig. 9. Effective sub-surface stress at load of 970 N (low). (a) Cylinder contact model (z/a = 5.5) (b) Numerical profile model (z/a = 5.5).

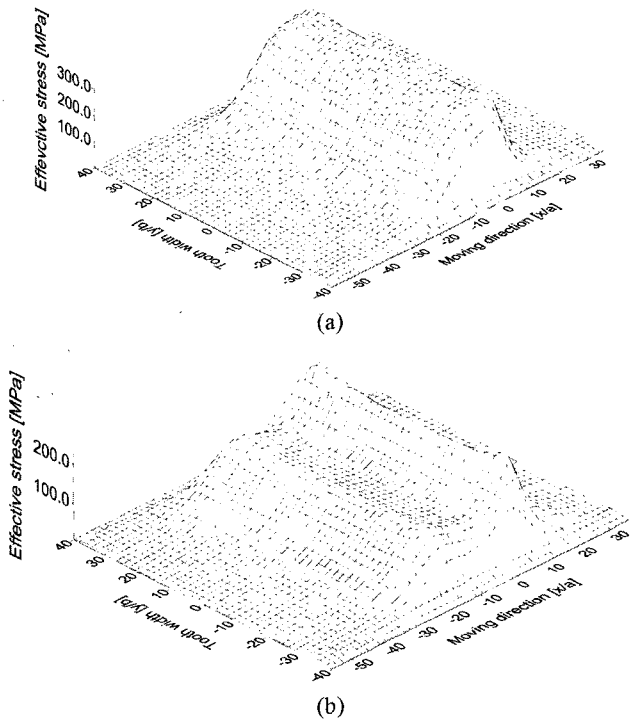

Fig. 10. Effective sub-surface stress at load of 1540 N (high). (a) Cylinder contact model (z/a = 7.5) (b) Numerical profile model (z/a = 4.0).

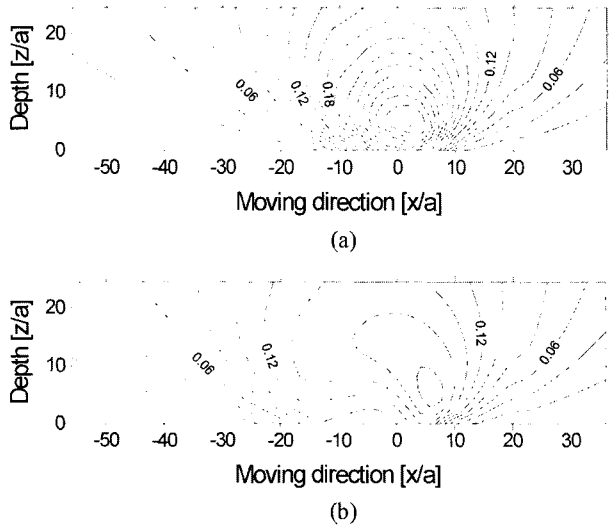

Fig. 11. Contour of σ_e/S on x-z plane beneath the surface at 970 N. (a) Cylinder contact model (y/b = 28) (b) Numerical profile model (y/b = 28).

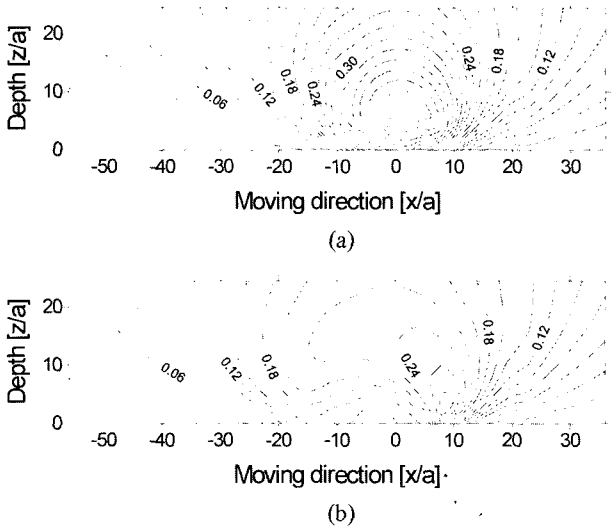

Fig. 12. Contour of σ_e/S on x-z plane beneath the surface at 1540 N. (a) Cylinder contact model (y/b = 28) (b) Numerical profile model (y/b = 28).

of the cylinder contact model and the contact area is kept wide even though the load is decreased. Therefore, the sub-surface stress of the numerical profile model for low load is far lower than that of the cylinder contact profile model.

The analysis results are summarized in Table 2.

Conclusions

The sub-surface stress field beneath the contact surface of the gear teeth was investigated for two kinds of tooth geometric profile models. The one is the conventional cylinder contact profile model, the other is the new numerical profile model.

Surface pressure distribution was obtained by using transient EHL analysis and it was applied to the input data of the sub-surface stress analysis. The difference of the surface pressure between the two profile models is that the numerical profile model has high pressure at the inlet region as well as pressure

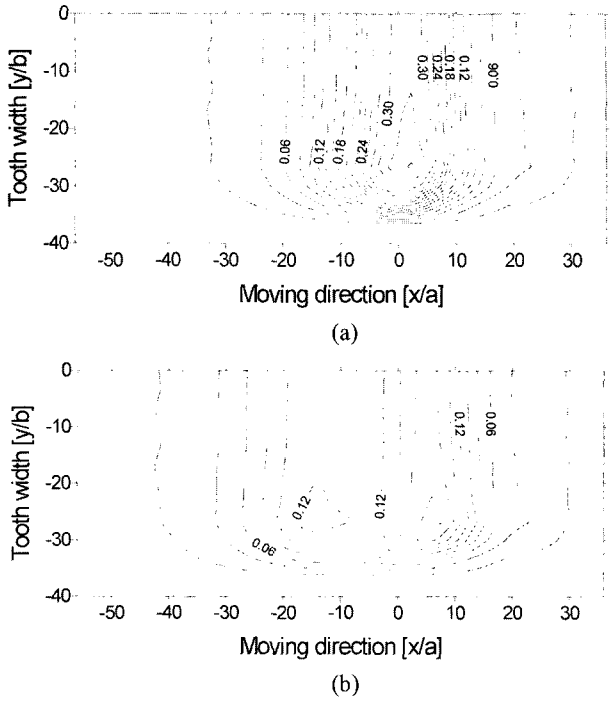

Fig. 13. Contour of σ_e/S on x-y plane beneath the surface at 970 N. (a) Cylinder contact model (Max. 0.343) (b) Numerical profile model (Max. 0.189).

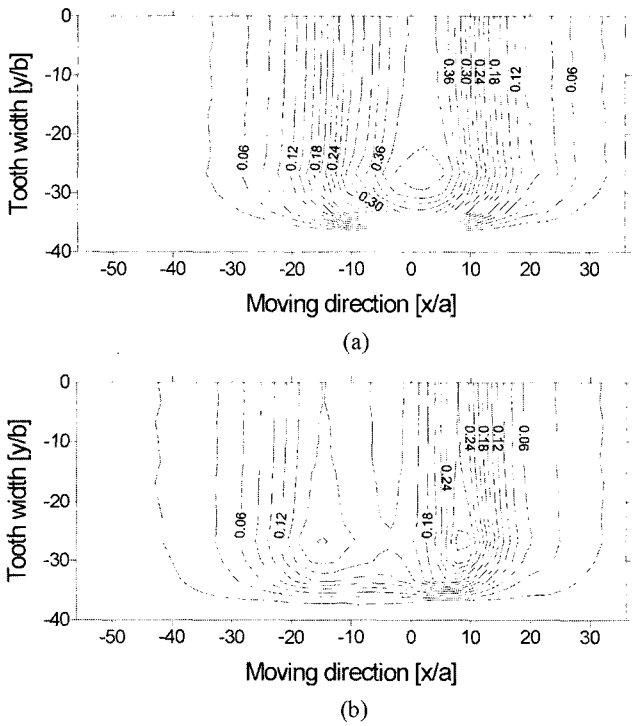

Fig. 14. Contour of σ_e/S on x-y plane beneath the surface at 1540 N. (a) Cylinder contact model (Max. 0.417) (b) Numerical profile model (Max. 0.290).

Table 2. Comparison of the analysis result

Load [N]	Tooth geometric profile model	Maximum surface pressure [MPa]	Maximum effective stress [MPa]	Position of maximum effective stress		
				z/a	*x/a*	*y/b*
970 (low)	Cylinder contact	526	286	5.5	2	28
	Numerical	314	158	5.5	6	28
1540 (high)	Cylinder contact	632	349	7.5	2	28
	Numerical	538	242	4	10	28

peaks at the outlet region whereas the cylinder contact model has only pressure peaks at the outlet region.

The sub-surface stress field was obtained by using Love's rectangular patch solution. The analysis results show that the sub-surface stress is quite dependent on both the surface pressure and the profile model. The maximum effective stress of the new model is lower than that of the old model. The depth where the maximum effective stress occurs in the new model is not proportional to the intensity of the external load. Because the analysis results could be utilized in life estimation of gears, design of tooth geometry or profiling, etc., a reasonable tooth profile model would be much helpful to improve the analysis accuracy.

Nomenclatures

a: half size of a rectangular patch in rolling and sliding direction [m]
b: half size of a rectangular patch in tooth width direction [m]
E: longitudinal modulus of elasticity [N/m^2]
H: dimensionless film thickness
h: film thickness [m]
h_g: geometrical clearance between gear tooth and pinion tooth [m]
n: number of rectangular patches on tooth surface
P: dimensionless pressure
p: pressure [N/m^2]
p_k: normal surface pressure on the contact surface [N/m^2]
R: equivalent radius [m]
R_i: radius of curvature of gear/ pinion tooth [m] (i = 1 for gear, i = 2 for pinion)
R_{bi}: base circle radius of gear/ pinion [m]
R_{oi}: addendum circle radius of the gear/ pinion [m]
R_{pi}: pitch circle radius of the gear/ pinion [m]
r_i: radius in polar coordinates [m]
S: yield strength of the gear material [N/m^2]
$s_{ij,k}$: stress component on the sub-surface due to surface pressure p_k [N/m^2]
T: dimensionless time
t time [s]
U: dimensionless velocity parameter
u: mean surface velocity [m/s]
v_i: surface velocity of the gear/ pinion tooth [m/s]
V: dimensionless normal squeeze velocity parameter
w: external load [N]
x: coordinate on the sub-surface in rolling and sliding direction
y: coordinate on the sub-surface in tooth width direction
z: coordinate on the sub-surface in depth direction
X, Y: dimensionless Cartesian coordinates
x_i, y_i: local Cartesian coordinates for gear/ pinion
Z: dimensionless viscosity-pressure index
Γ: Boussinesq's 3-dimensional logarithmic potential
Λ: Newtonian potential of surface distribution
α: pressure angle [rad]
η: viscosity [Ns/m^2]
η_0: viscosity at p=0 [Ns/m^2]
$\bar{\eta}$: dimensionless viscosity
θ_i: rotation angle of the gear/ pinion [rad]
ρ: density [Ns^2/m^4]
ρ_0: density at p=0 [Ns^2/m^4]
$\bar{\rho}$: dimensionless density
ω_i: angular velocity of the gear/ pinion [rad/s]
ν: Poisson's ratio
ξ,ζ: coordinates on the contact surface
σ_e: von Mises' effective stress [N/m^2]
σ_{ij}: sub-surface stress [N/m^2]

References

1. Rao, S. S. and Tjandra, Muljadi, "Reliability-based design of automotive transmission systems," Reliability Engineering & System Safety, Vol. 46, pp. 159-169, 1994.
2. Yang, Q. J., "Fatigue test and reliability design of gears," International Journal of Fatigue, Vol. 18, pp. 171-177, 1996.
3. Johnson, K. L., "Contact mechanics," pp. 11- 26, 1985.
4. Fuchs, H. O. and Stephens, R. I., "METAL FATIGUE IN ENGINEERING," J. WILEY & SONS, pp. 66-75.
5. Hertz. H, Miscellaneous Papers on the contact of elastic solids, Translation by D. E. Jones, McMillan, London, 1986
6. Hamrock, B. J. Fundamentals of Fluid Film Lubrication, McGRAW-HILL, pp. 141-165, 1994.
7. Dowson, D. and Higginson, G. R., Elastohydrodynamic lubrication, the Fundamentals of Roller and Gear Lubrication,Pergamon, Oxford, 1966.
8. Roelands, C. J. A, Correlational Aspects of the Viscosity-Temperature-Pressure Relationship of Lubricating Oils, Doctoral thesis, Technische Hogeschool te Delt, Netherlands, 1966.
9. Love, A. E. H., "Stress Produced in a Semi- Infinite Solid by Pressure on Part of the Boundary," Phil. Trans. Royal Society, A228, pp. 377-420, 1929.
10. Koo, Y. P., Cho, Y. J., Lee, D. W., 2002, "3-Dimensional Elastohydrodynamic Lubrication Analysis on the Cam-Roller Contact with Consideration of Roller Profiling, *JSME*

International Journal, Vol. 45(C), pp. 316-322.
11. Larsson, R. Transient non-Newtonian elastohydrodynamic lubrication analysis of an involute spur gear, Wear 207, pp. 67-73, 1997.
12. A. P. Boresi, "Advanced Mechanics of Materials